MICROBIOLOGY

Structural basis for subversion of host cell actin cytoskeleton during *Salmonella* infection

Biao Yuan[1,2,3], Jonas Scholz[4], Jiri Wald[1,2,3], Roland Thuenauer[2,5,6], Rory Hennell James[1,2,3], Irina Ellenberg[7], Sabine Windhorst[7], Jan Faix[4], Thomas C. Marlovits[1,2,3]*

Secreted bacterial type III secretion system (T3SS) proteins are essential for successful infection by many human pathogens. Both T3SS translocator SipC and effector SipA are critical for *Salmonella* infection by subversion of the host cell cytoskeleton, but the precise molecular interplay between them remains unknown. Here, using cryo–electron microscopy, we show that SipA binds along the F-actin grooves with a unique binding pattern. SipA stabilizes F-actin through charged interface residues and appears to prevent inorganic phosphate release through closure of the "back door" of adenosine 5′-triphosphate pocket. We also show that SipC enhances the binding of SipA to F-actin, thus demonstrating that a sequential presence of T3SS proteins in host cells is associated with a sequence of infection events—starting with actin nucleation, filament growth, and stabilization. Together, our data explain the coordinated interplay of a precisely tuned and highly effective mechanism during *Salmonella* infection and provide a blueprint for interfering with *Salmonella* effectors acting on actin.

INTRODUCTION

In eukaryotic cells, the structure and dynamics of the cellular actin network are tightly regulated in space and time by a large number of actin-binding proteins (ABPs) (*1*). Nevertheless, upon bacterial infection, the host cell cytoskeleton is rapidly subverted by bacterial effectors, including ABPs, which are essential for invasion and pathogenesis by many microbial pathogens (*2*). The human pathogen *Salmonella enterica* serotype Typhimurium (*Salmonella typhimurium*) uses the type III secretion system (T3SS) encoded chromosomally on the *Salmonella* pathogenicity island-1 (SPI-1), a molecular machine used to secrete a cocktail of specific proteins in a hierarchical sequence into host cells to promote host cell entry at the invasion site by inducing local membrane ruffling (*3*). *Salmonella* T3SS effector SopE, acting as a guanine nucleotide exchange factor mimic, can directly activate Rho guanosine triphosphatases to induce membrane ruffling, while the phosphoinositide phosphatase SopB can recruit sorting nexin protein SNX18 to facilitate membrane ruffling formation (*4*, *5*).

Two particular *Salmonella* T3SS substrates, SipC and SipA, are delivered into host cells to manipulate the cell cytoskeleton at bacterial attachment sites during bacterial invasion (*6*). Both contain actin-binding domains that share no discernible sequence similarity with other known ABPs or with each other. Upon T3SS-mediated secretion, SipC integrates into the host cell membrane and assembles together with SipB, the second component of the translocon, into a pore-like structure that presumably serves as an interaction site at the tip of T3SS (*7*, *8*) and provides the structural scaffold for effector protein translocation into cells. SipC has been hypothesized to play a central role at these focal infection sites due to its actin bundling activity (*6*, *9*, *10*), its ability to nucleate actin via its soluble C-terminal domain (*9*), and its stimulation of focal plasma membrane expansion by recruiting host cell exocytotic vesicles through binding to the exocyst complex (*11*). Furthermore, SipC is also able to recruit lysosome-associated membrane protein 1 to prevent targeting of invading bacterial cells to lysosomes (*12*).

The translocon pore is a prerequisite for delivery of late effectors, which are thought to be transported through the central part of the pore (*13*). SipA is the first of the late effectors to be delivered (*14*) and is cleaved by host cell caspase-3 into two functional fragments (*15*). The N-terminal SipA fragment can recruit the host soluble *N*-ethylmaleimide–sensitive fusion protein attachment protein receptors components to *Salmonella*-containing vacuoles (SCVs) and promotes *Salmonella* survival by mimicking the early endosome (*16*). Previously, low-resolution electron microscopy (EM) maps of F-actin-SipA show that the C-terminal SipA fragment binds along the F-actin groove in an 1:1 molar ratio and the two flexible arms of SipA connect the two long actin helical strands to stabilize actin filaments as a molecular stapler (*17*, *18*). Noteworthy, SipA has a much greater stabilization effect on F-actin stabilization than the bicyclic peptide phalloidin, a commonly used F-actin stabilizer (*19*). Cooperation between SipA and SipC likely through the actin nucleation and bundling activity leads to the formation of large actin bundles that generate filopodial-like membrane protrusions at the invasion site (*6*). However, the mechanistic interplay between these two bacterial proteins, in which SipA resides as a soluble protein within the host cell cytoplasm and SipC is restricted to the host cell plasma membrane, remains unknown, especially in the context of the numerous other cellular ABPs.

To unravel how SipA and SipC subvert the cellular cytoskeleton, we used cryo-EM and single-particle analysis of polymerizing actin filaments in vitro. Unlikely to the previous models, on the basis of low-resolution EM maps reconstructed from negative-stain EM data of F-actin-SipA, our near atomic resolution cryo-EM map of F-actin-SipA reveals that the binding of SipA is accomplished by a central globular domain and a flanking C-terminal domain,

[1]University Medical Center Hamburg-Eppendorf (UKE), Institute of Structural and Systems Biology, Hamburg, Germany. [2]Centre for Structural Systems Biology (CSSB), Hamburg, Germany. [3]Deutsches Elektronen-Synchrotron Zentrum (DESY), Hamburg, Germany. [4]Institute for Biophysical Chemistry, Hannover Medical School, Hannover, Germany. [5]Technology Platform Light Microscopy (TPLM), University of Hamburg, Hamburg, Germany. [6]Technology Platform Microscopy and Image Analysis (TP MIA), Leibniz Institute of Virology (LIV), Hamburg, Germany. [7]University Medical Center Hamburg-Eppendorf (UKE), Institute for Biochemistry and Signal Transduction, Hamburg, Germany.
*Corresponding author. Email: marlovits@marlovitslab.org

both of which are responsible for the unique binding ratio: one SipA to two actin subunits. The efficiency of SipA binding is improved by the translocon component SipC. The binding of SipA leads to a marked stabilization of the filaments even under substoichiometric conditions, underscoring the development of an elegant and efficient infection strategy at the molecular level during the evolution of *Salmonella* pathogenesis.

RESULTS

SipA constantly modulates the actin network during *Salmonella* infection

To gain insights into the role of SipA-mediated reorganization of the host cell actin network, we first examined the localization of SipA and actin during *Salmonella* infection. HeLa cells were challenged with *S. typhimurium* cells expressing a chromosomally encoded SipA variant with a C-terminal hemagglutinin (HA)–tag (*20*), and the distribution of the bacterial effector SipA and the associated cellular actin network was monitored using fluorescence microscopy. Four different distribution patterns could be distinguished between the 15- and 30-min time points (Fig. 1A and fig. S1A): SipA molecules were evenly distributed inside a *Salmonella* cell, which is attached to a HeLa cell (pattern 1); SipA colocalized with F-actin close to the plasma membrane, and *Salmonella* cells attached to HeLa cells (pattern 2); the signal for SipA was detected largely outside of the bacterial cells but remained in the immediate vicinity of the SCV (pattern 3); and the SCV-exposed SipA colocalized with F-actin (pattern 4). The populations of patterns 1 and 3 were both less than 10% of the overall population and marginally changed between the 15 min and 30 min after start of the experiment (fig. S1B). Most *Salmonella* cells that are not in the process of invading the host cell are washed away during the immunostaining procedure, leading to the small proportion of cells in pattern 1. The observation that pattern 4 becomes predominant after 30 min suggests that pattern 4 represents the latest stage of infection (fig. S1B).The nanomolar binding affinity of SipA to actin filaments (*3*) suggests that SCV surface–exposed SipA is able to quickly recruit surrounding actin molecules, which leads to a rapid transition from pattern 3 to pattern 4. Consequently, the fraction of pattern 3 at the time of imaging is always small.

On the basis of these observations, we propose a model for the invasion process of *Salmonella*. At first, before invasion, SipA molecules remain inside bacterial cells (stage 1: SipA loading stage). Shortly after attachment to HeLa cells, *Salmonella* starts injecting SipA (*21*), which is colocalized with F-actin close to the plasma membrane (stage 2: SipA injection stage). After the bacterial cell is internalized and resides in an SCV, SipA is constantly secreted via SPI-1 T3SS (*22*) (stage 3: SipA SCV injection stage). Last, SCV-exposed SipA recruits new F-actin, establishing a distinct actin network around the SCVs (stage 4: SCV actin network stage).

SipA binds to F-actin in a unique binding pattern

The fact that, during infection, a single actin-binding domain of SipA (amino acids 434 to 685) is released into the host cell cytoplasm by caspase-3 suggests that all the observed intracellular stages of infection are caused by the same mechanism of SipA binding to actin. On the basis of earlier structural and biochemical data, it has been hypothesized that SipA functions as a molecular staple in which two nonglobular arms emanating from the central globular domain of SipA tether two actin subunits from two opposing strands of the same filament (*17*, *18*). A repeated arrangement would then affect filament polymerization and stabilization. However, the atomic details of such a mechanism have not yet been resolved either by x-ray crystallography or cryo-EM. Moreover, in an in infectio context, it is likely that the ratio of (cleaved) SipA molecules to actin molecules varies, is nonstoichiometric, and may influence actin stabilization.

To examine the importance of the stoichiometry of SipA for F-actin stabilization, we first measured the effect of SipA$^{\beta}$ (SipA$_{426–685}$) concentration on actin depolymerization as a proxy for filament stabilization. SipA$^{\beta}$, representing the C-terminal fragment of SipA cleaved by caspase 3 (*15*), strongly stabilized filaments at a molar ratio of 1:1 and was evidently effective even at a molar ratio of 1:100 (Fig. 2A). This demonstrates that SipA$^{\beta}$ is capable of modulating the cellular actin network, supporting the idea of highly specialized and effective molecules during infection operating at substoichiometric concentrations.

To gain direct structural insights into the interaction of SipA with F-actin, we determined the structure of SipA$^{\beta}$ bound to F-actin by cryo-EM (fig. S2, A to C). To our surprise, we found that SipA$^{\beta}$ interacts with F-actin in a unique, alternating binding pattern by which its globular domain is located in the F-actin groove between the two opposing actin strands, leaving out every other binding pocket (fig. S2D). We also noticed that the complex could not be refined to resolutions better than 5 Å at the SipA$^{\beta}$ region, which we attribute to a nonuniform binding pattern and the overall low SipA occupancy (21.2%; fig. S2B). Despite the fact that the structure at this resolution is distinct from previous work (*17*, *18*), our attempt to understand atomic details of the binding interface required us to use a new construct to improve the resolution. Thus, we generated a smaller version of SipA (SipA$^{\alpha}$: SipA$_{497–669}$) (*17*) omitting regions that were predicted to be largely disordered using IUPred3 (*23*) (fig. S2E) and resolved the structure of SipA$^{\alpha}$–F-actin to an overall resolution of 2.6 Å (Fig. 2, B and C, and fig. S3, A and B). The central and heart-shaped domain of SipA was well resolved by cryo-EM (fig. S3C), and it fits well inside one F-actin pocket formed by three adjacent actin subunits from two helical strands with the C-terminal arm extending toward the adjacent F-actin pocket in the direction of the pointed end (PE) of the filament, preventing a second heart-shaped domain from entering this pocket (Fig. 2C). Similarly to SipA$^{\beta}$, the shorter SipA$^{\alpha}$ molecules bind in a unique molar ratio of 1:2 along the groove between the two helical strands of F-actin, a binding region that is used to stabilize filamentous actin by unrelated molecules such as the bicyclic peptide phalloidin from the death cup mushroom *Amanita phalloides* (*24*) (molar ratio 1:1) or by nebulin, a long, multirepeat protein present in skeletal muscle within myofibrils (*25*) (molar ratio per super repeat, 1:1). The fact that this specific binding site is not used by the majority of known host ABPs such as filamin A, T-plastin, or cofilin allows SipA-mediated actin network modulation during bacterial infection (Fig. 2D) (*26–28*).

Robust interaction sites between SipA and F-actin

As an F-actin stabilizer, SipA binds with a footprint that contacts three adjacent G-actin subunits and contains multiple charged residues (Fig. 3A and table S1). We constructed SipA$^{\beta}$ variants with amino acid substitutions designed to probe the interaction

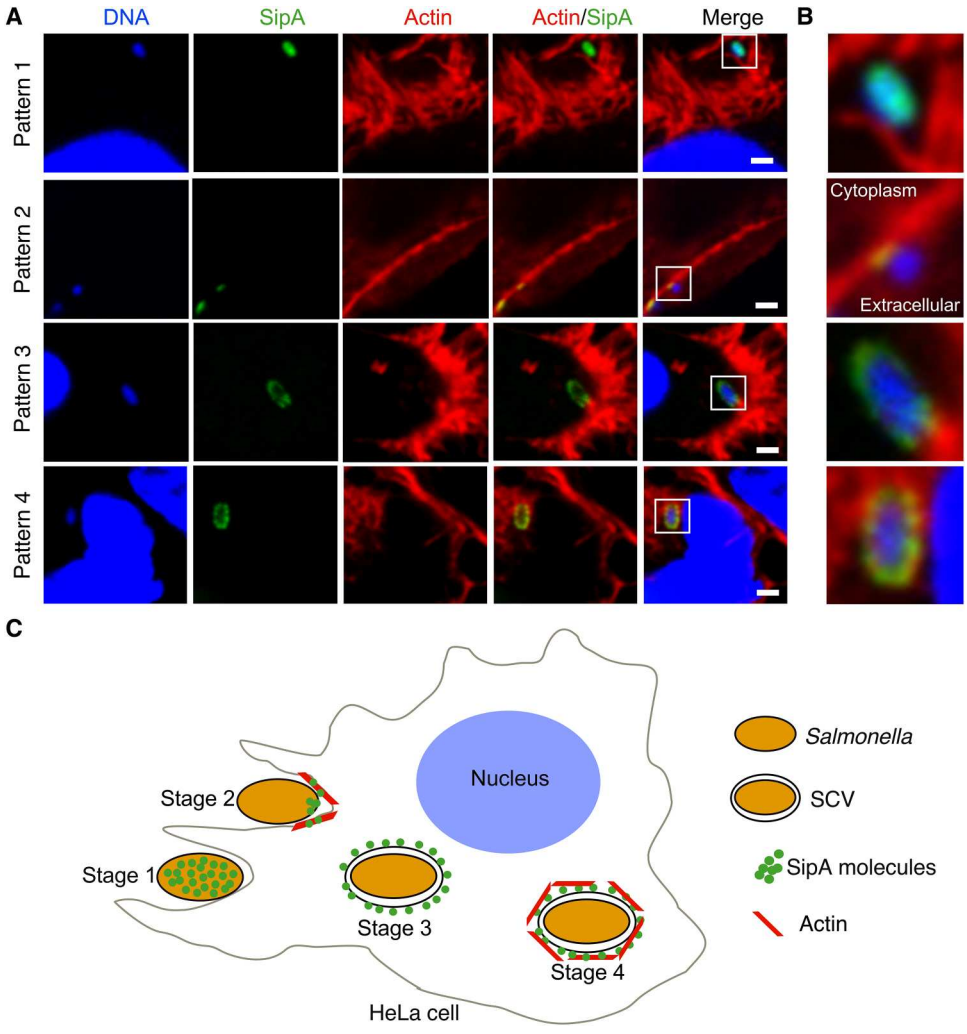

Fig. 1. SipA differentially modulates the actin network during *Salmonella* host cell entry. (**A**) Four different infection patterns based on SipA localization were discernable in wild-type *Salmonella* M1223 expressing chromosomally HA-tagged *sipA* that were allowed to enter HeLa cells for 15 min. DNA (blue), SipA-HA (green), and actin (red) were stained with 4′,6-diamidino-2-phenylindole (DAPI), mouse anti-HA and anti-mouse AF488, and phalloidin-Atto-647N, respectively. Images were recorded with a spinning disc confocal microscope, and representative *x-y* sections are shown. White boxes indicate magnified regions in (B). Scale bars, 2 μm. (**B**) Zoomed-in views of bacterial cells with different distribution patterns in (A). (**C**) Schematic diagram of the model of *Salmonella* invasion process.

interfaces and their effect on stabilizing F-actin without disrupting binding. We selectively substituted two or three charged interface residues at a time in different regions of the heart-shaped domain and tested their binding ability of the variant proteins by cosedimentation with F-actin. The SipA$^{\beta}$ variants were designated M1 (H536E/H539E), M2 (R551E/K552E/E555R), M3 (R565E/R566E/D569R), M4 (K618E/E621R), and M5 (R628E/E629R) (Fig. 3A and table S2). M1 to M5 bound F-actin at similar ratios to wild-type SipA$^{\beta}$ suggesting redundancy of the different interfaces (Fig. 3B and fig. S4A). Unexpectedly, all five SipA$^{\beta}$ variants were impaired in stabilizing F-actin during depolymerization as compared to wild-type SipA$^{\beta}$, albeit to varying degrees, with variants M2 and M5 exhibiting the weakest effect of filament stabilization (Fig. 3C and fig. S4B). To determine whether stabilization of F-actin by SipA$^{\beta}$ is part of the *Salmonella* infection mechanism, we generated two *S. typhimurium* strains with mutations in *sipA* encoding the same substitutions as SipA$^{\beta}$ variants M2 and M5, denoted as *sipA* M2 and *sipA* M5, respectively, and performed infection and colocalization assays. Although the two SipA variant proteins were still associated with the cellular actin network (Fig. 3D), the invasion rates of the M2 and M5 mutant strains were attenuated compared to wild-type *S. typhimurium* (Fig. 3E), suggesting that stabilization of actin filaments during infection contributes to *Salmonella* invasion.

SipA$^{\beta}$ does not affect nucleation or elongation but completely inhibits cofilin-mediated filament severing

To assess the effect of SipA$^{\beta}$ on actin assembly in real time, we compared the spontaneous birth and elongation of actin filaments from 1 μM G-actin in the absence or presence of super folder green fluorescent protein (sGFP)–tagged SipA$^{\beta}$ in vitro by total internal reflection fluorescence (TIRF) microscopy (Fig. 4A and movie S1). Notably, at a concentration of 1 μM, SipA$^{\beta}$ fully decorated the growing filaments and induced the formation of flexible bundles

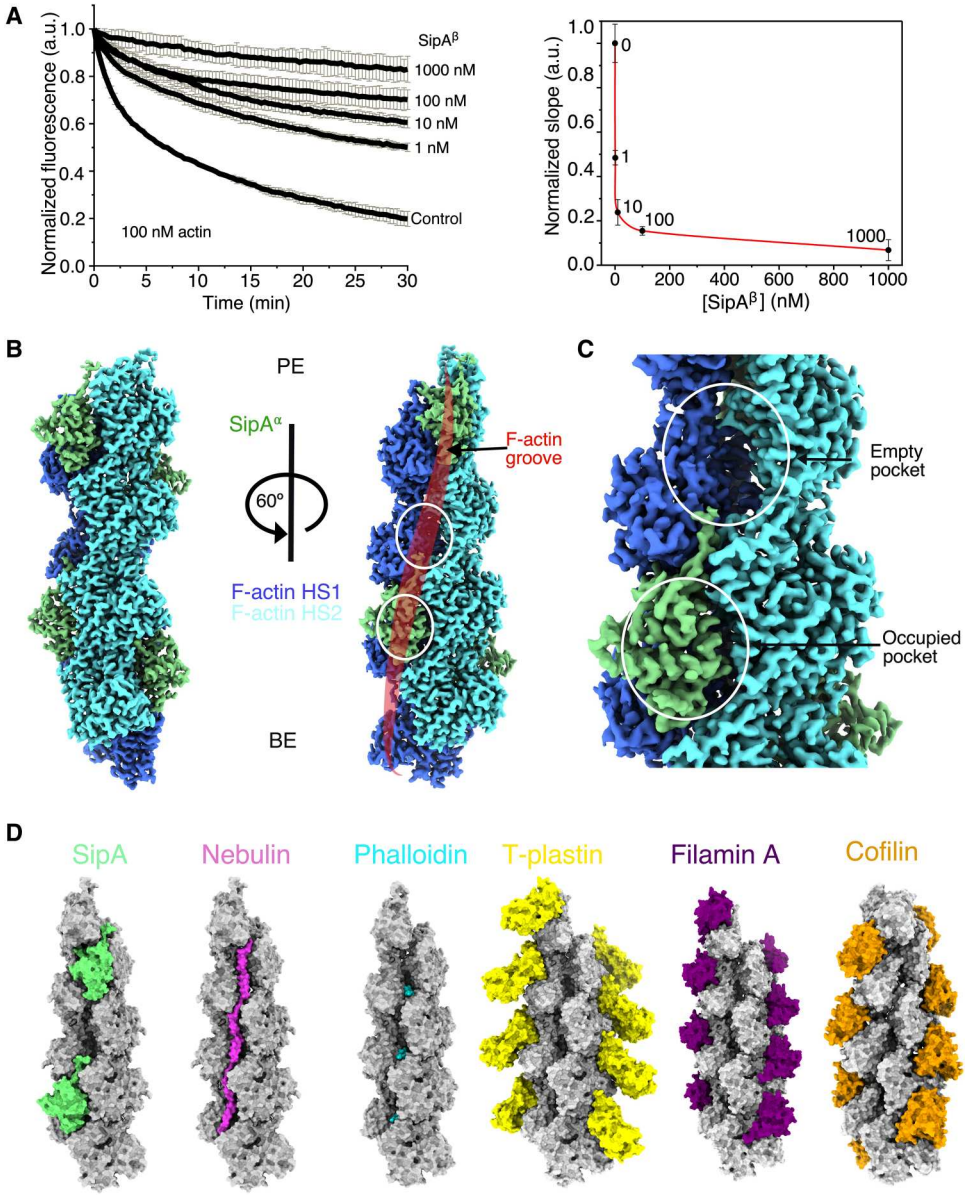

Fig. 2. SipA stabilizes F-actin under substoichiometric conditions and binds in a unique pattern. (**A**) Time course of F-actin depolymerization induced by dilution in the presence of SipA$^{\beta}$ (left). SipA$^{\beta}$-free buffer was used as negative control (left). Normalized and averaged initial slopes of dilution-induced depolymerization assays were plotted against the concentration of SipA$^{\beta}$ (right). Data points and error bars indicate means ± SD from three independent experiments. a.u., arbitrary units. (**B**) Cryo-EM structure of SipA$^{\alpha}$ bound to F-actin. Two F-actin helical strands decorated by SipA$^{\alpha}$ are colored dark blue and light blue, and SipA$^{\alpha}$ molecules are shown in light green. The pointed end (PE), barbed end (BE), F-actin groove, and F-actin pocket are indicated. HS, helical strand. (**C**) Zoomed-in view of SipA$^{\alpha}$ well-anchored inside the F-actin pocket. The adjacent empty pocket and the occupied pocket are indicated. (**D**) Surface representations of F-actin (gray) with different interaction partner: nebulin–F-actin [Protein Data Bank (PDB): 7QIM] (*25*), phalloidin–F-actin (PDB: 7BTI) (*24*), filamin A–F-actin (PDB: 6D8C) (*27*), T-plastin–F-actin (PDB: 7R94) (*26*), and cofilin–F-actin (PDB: 6VAO) (*28*).

but did not affect their nucleation or elongation (Fig. 4, B and C, and fig. S5), strongly suggesting that SipA$^{\beta}$ does not affect actin assembly but rather associates with the filaments after their formation. In an attempt to better visualize the association of SipA$^{\beta}$ with the filaments, we then analyzed filament assembly in the presence of substoichiometric concentrations of GFP-SipA$^{\beta}$ (0.002 μM). Unexpectedly, even at this very low concentration, sGFP-SipA$^{\beta}$ was immediately visible on the filaments, suggesting a high affinity in the low-nanomolar or subnanomolar range and/or a fast association rate constant. As a consequence, within a short period of time, sGFP-SipA$^{\beta}$ was completely depleted from solution, which then led to the growth of entirely undecorated filaments, highlighting the irreversible association of SipA$^{\beta}$ with filaments (movie S1).

To explore whether the strong association of SipA$^{\beta}$ with the actin filaments interferes with the binding and activity of other ABPs, we then performed TIRF microscopy experiments with α-actinin 4, T-plastin, fascin, and cofilin I, respectively. Cross-linking and bundling of filaments induced by α-actinin 4 and T-plastin were not

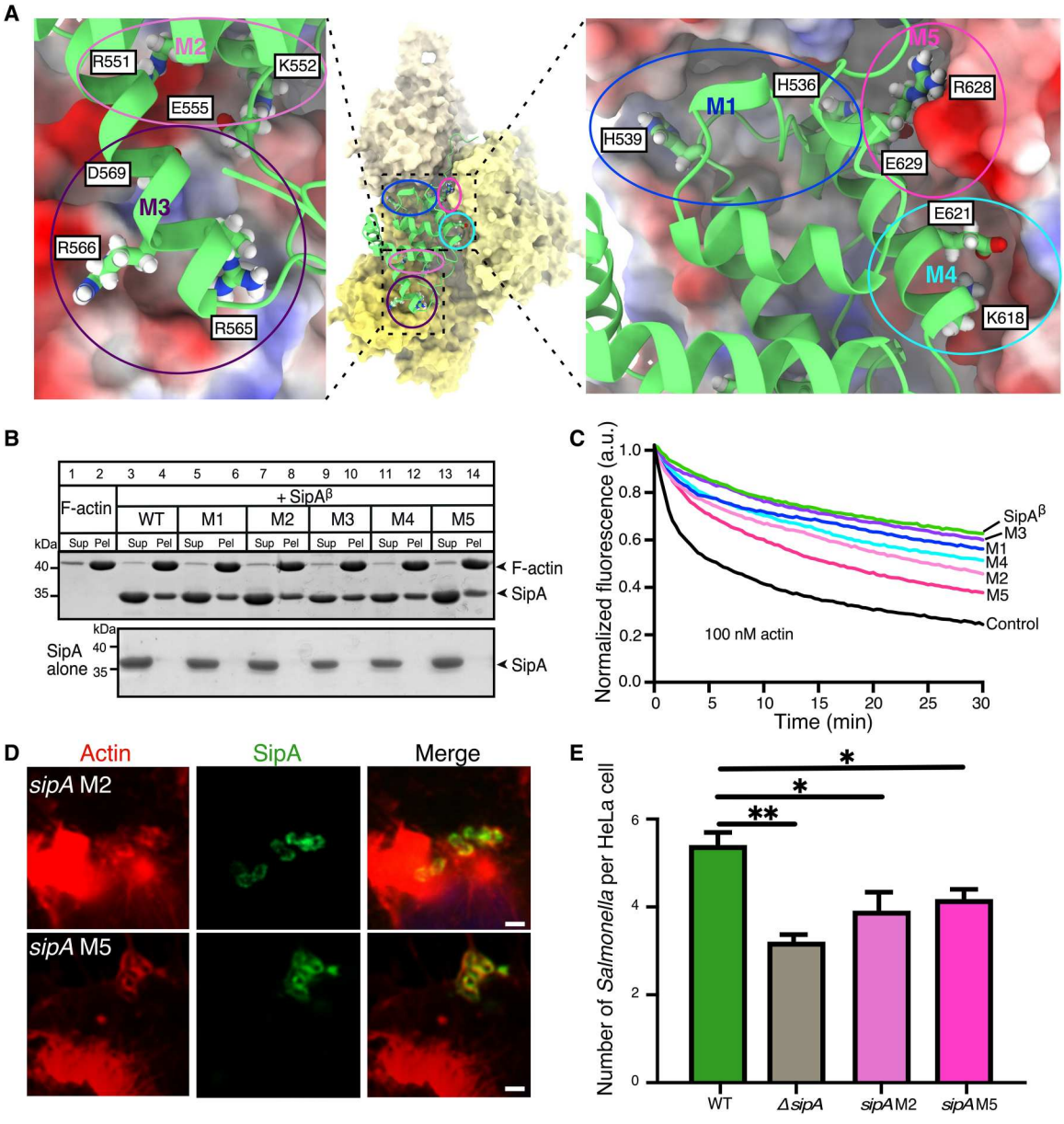

Fig. 3. Characterization of F-actin stabilization by SipA and its role in *Salmonella* infection. (**A**) Electrostatic interactions between SipA and F-actin. The charged interface residues substituted in further studies are shown in stick representation and labeled (M1, SipA$^{\beta}_{H536E/H539E}$; M2, SipA$^{\beta}_{R551E/K552E/E555R}$; M3, SipA$^{\beta}_{R565E/R566E/D569R}$; M4, SipA$^{\beta}_{K618E/E621R}$; M5, SipA$^{\beta}_{R628E/E629R}$). The actin subunits are colored on the basis of electrostatic potential from positive charge (blue) to negative charge (red) in ChimeraX 1.3. In the middle panel, three actin subunits are shown in surface representation three shades of yellow, and SipA$^{\alpha}$ is shown in cartoon representation. (**B**) Substitution of a few charged residues did not interfere with F-actin binding. SipA$^{\beta}$ and the variant proteins M1 to M5 were incubated with preassembled F-actin for 2 hours at room temperature (RT) before ultracentrifugation at 150,000*g* for 30 min. The supernatants (Sup) and pellets (Pel) were analyzed by SDS–polyacrylamide gel electrophoresis (PAGE). (**C**) Time course of F-actin depolymerization induced by dilution in the presence of 10 nM SipA$^{\beta}$ or variants with charged residue substitutions (M1 to M5). SipA$^{\beta}$-free buffer was used as negative control. (**D**) *Salmonella* mutants *sipA* M2 and *sipA* M5 colocalize with F-actin in vivo. HeLa cells were infected with *Salmonella* strains expressing chromosomally encoded SipA-HA variants with the M2 or M5 substitutions for 30 min before immunostaining. SipA-HA and actin are shown in green and red, respectively. Images were recorded with a spinning disc confocal microscope. Scale bars, 2 μm. (**E**) *Salmonella* mutants *sipA* M2 and *sipA* M5 interfered with *Salmonella* invasion. The total number of invading bacterial cells per HeLa cell was quantified from spinning disc confocal image stacks. The average number of HeLa cells used for quantification for each condition from three independent experiments were 102 [wild-type (WT)], 116 (Δ*sipA*), 163 (*sipA* M2), and 96 (*sipA* M5). *$P \leq 0.05$ and **$P \leq 0.01$.

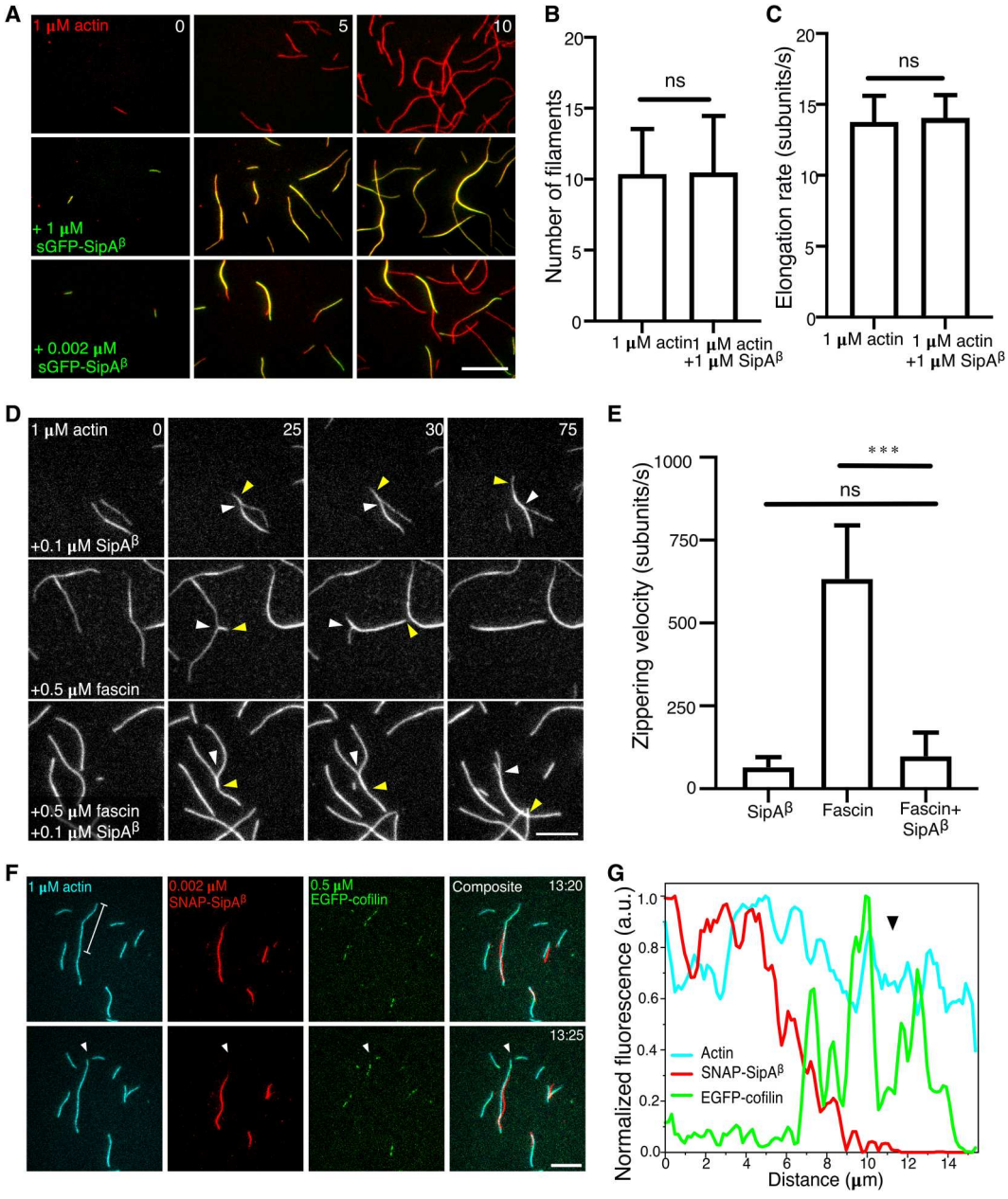

Fig. 4. SipA$^{\beta}$ perturbs fascin and cofilin functions but does not contribute to actin nucleation and filament elongation. (**A**) TIRF microscopy images of actin assembly in the absence or presence of sGFP-SipA$^{\beta}$. Time scale: minutes. Scale bar, 10 μm. (A) corresponds to movie S1. (**B** and **C**) Quantification of filament nucleation and elongation rates from TIRF microscopy movies as shown in (A). Bars represent means + SEM of 30 measured filaments from three independent experiments. (**D**) Polymerization of actin in the presence of SipA$^{\beta}$ or fascin or both proteins. Time-lapse TIRF microscopy micrographs illustrating the "zippering" of adjacent, parallel actin filaments. The beginning of the forming bundle is marked with a yellow arrowhead, and the filament fork at the moving end of the crosslinked F-actin bundle is marked with a white arrowhead. Time scale: seconds. Scale bar, 10 μm. (D) corresponds to movie S5. (**E**) Quantification of zippering velocity. The length of the zippered region was measured over time. ***$P \leq 0.001$. ns, not significant. (**F**) SipA$^{\beta}$-decorated actin filaments are resistant to cofilin-mediated severing. Representative time-lapse micrographs of triple-color TIRF microscopy assays used for analysis of cofilin-mediated severing in the presence of low concentrations of SipA$^{\beta}$ before or immediately after a severing event (white arrowheads). Polymerization of 1 μM G-actin (cyan) in the presence of 0.002 μM SNAP-tagged SipA$^{\beta}$ (red) and 0.5 μM EGFP-cofilin I (green). Time scale: second. Scale bar, 10 μm. (F) corresponds to movie S6. (**G**) Fluorescence intensity profile analysis used to determine the position of the filament cleavage site relative to normalized fluorescence intensities of SNAP-tagged SipA$^{\beta}$ versus EGFP-cofilin along a section of the filament (white line) as shown in (F). Note that cofilin I decoration and severing (black arrowhead) occur exclusively in a region of the filament that lacks or is largely devoid of SipA$^{\beta}$.

noticeably perturbed by SipA$^{\beta}$, confirming that these ABPs engage different binding sites on the F-actin from SipA$^{\beta}$ (movies S2 and S3). In contrast, the formation of the extremely rigid F-actin bundles induced by fascin was strongly impaired by SipA$^{\beta}$. These bundles were more flexible than in the absence of SipA$^{\beta}$ and had splayed ends, a behavior never observed with fascin alone (movie S4). Notably, the zippering velocity of bundles in the presence of fascin was reduced more than sixfold in the presence of SipA$^{\beta}$ from 633 ± 162 (mean ± SD) to 98 ± 72 subunits/s (Fig. 4, D and E, and movie S5). Therefore, SipA′s interference with fascin-mediated actin bundling could lead to a larger pool of individual actin filaments that can be stabilized.

Last, we analyzed the binding of enhanced GFP (EGFP)-labeled cofilin I to F-actin filaments and subsequent filament severing in the absence or presence of SipA$^{\beta}$. As expected, cofilin I (0.5 μM) first bound preferentially to aged adenosine 5′-diphosphate (ADP)–F-actin in a discontinuous fashion and subsequently decorated the entire filament except for the growing tip due to cooperative binding (*29*), with filament severing occurring at the interface of decorated and nondecorated regions of the filaments (movie S6). Notably, in the presence of both cofilin I (0.5 μM) and substoichiometric untagged SipA$^{\beta}$ (0.1 μM), cofilin I binding to F-actin filaments and, hence, filament severing was completely abolished (movie S6), which is consistent with a previous study using fluorescence imaging of fixed specimens and sedimentation assays (*3*). To allow simultaneous visualization of all proteins in the reaction, we used triple-color TIRF microscopy using Atto655-spiked G-actin, EGFP–cofilin I, and surface 549–labeled SNAP-SipA$^{\beta}$. As shown in Fig. 4 (F and G), EGFP-cofilin I and SNAP-SipA$^{\beta}$ bound to actin filaments in distinct, largely nonoverlapping regions, with filament severing occurring only between bare and cofilin-decorated segment boundaries devoid of SipA$^{\beta}$ (movie S7).

Together, our data are consistent with the view that, after T3SS-mediated translocation in host cells, the late effector SipA both maintains a larger pool of actin filaments by interference with fascin-mediated actin bundling and cofilin I filament severing and stabilizes actin filaments. Together with the observation of the cooperation between SipC and SipA from previous work (*6*, *9*), our results raise the question of whether SipA acts alone or in conjunction with SipC on actin. SipC is a substrate of the T3SS that occupies an intermediate position in the hierarchical secretion sequence, is anchored as part of the membrane-associated translocon, and contains an actin-binding domain at the C terminus (SipCc: SipC$_{200–409}$) that is involved in actin filament nucleation.

SipC enhances SipA decoration of ADP-P$_i$ F-actin

To examine the effect of SipC on the binding of SipA to actin, we incubated G-actin with SipA$^{\beta}$ and SipCc (fig. S6A) under the same conditions used for determining the actin-bound structures of SipA$^{\beta}$ and SipA$^{\alpha}$ as shown in Fig. 2C and fig. S2D. Notably, during image processing of our cryo-EM data, we noticed that in the presence of SipCc, actin segments were completely decorated by SipA$^{\beta}$ in the 1:2 stoichiometry (98.8% occupancy), a behavior we only observed in the absence of SipCc for the shorter SipA$^{\alpha}$ construct (92.2% occupancy), but not with the longer in vivo–like SipA$^{\beta}$ construct (21.2% occupancy) (Fig. 5A). This suggests that SipCc promotes the binding of SipA$^{\beta}$ to actin filaments, which would lead to increased occupancy of actin filaments by SipA$^{\beta}$ at the site of invasion. The mechanism by which SipCc promotes SipA$^{\beta}$ binding to actin filaments remains unclear, as no SipCc density was visible in our reconstructions (fig. S6, B and C). SipCc is predicted to be largely unstructured (fig. S6D), and the resulting flexibility could enable repeated nucleation of actin polymerization.

Despite the lack of SipCc density, the addition of SipCc allowed us to resolve the structure of actin-bound SipA$^{\beta}$ to near-atomic resolution (Fig. 5B and fig. S6C). The SipA$^{\beta}$ construct includes the entire C-terminal fragment produced by caspase-3 cleavage of full-length SipA, so this structure represents the complete SipA–F-actin complex. We found that the N-terminal arm remains unstructured and the fully resolved C-terminal arm (residues 660 to 685) extends deep inside the F-actin pocket (Fig. 5, B and C). This binding only marginally influences the conformation of the central heart-shaped domain [root mean square deviation (RMSD), 0.77 Å; Fig. 5D]. The binding interface for the C-terminal arm is located in the vicinity of the binding interface of the commonly used F-actin stabilizer phalloidin (*24*), indicating that the C-terminal arm could contribute to F-actin stabilization. SipA$^{\beta}$ stabilizes F-actin more strongly than SipA$^{\alpha}$, which does not contain the extended arms (Fig. 5E).

Unexpectedly, our structural analysis also revealed that SipA binds exclusively to the "young" ADP–inorganic phosphate (P$_i$) actin (fig. S6E) as opposed to cofilin I, which preferentially binds aged ADP-actin and at a different binding site than SipA (*28*). This explains the differential decoration observed in our TIRF microscopy measurements (Fig. 4F) and supports the idea that SipA binds shortly after SipC-catalyzed actin nucleation to stabilize filaments. Notably, the fact that our structure was determined in a buffer lacking phosphate, suggests that the phosphate visible in SipA-bound young actin originates from adenosie 5′-triphosphate (ATP) hydrolysis. This is in contrast to earlier studies where it cannot be ruled out that the phosphate originates from phosphate-containing buffers (*30*, *31*). Furthermore, our structural analysis revealed that the "back door" formed by R177, N111, H73, and G74 (*30*) is stabilized in a closed conformation in the presence of SipA (Fig. 6, A and B). This suggests that SipA binds to young actin filaments and keeps them in a young state by preventing the release of inorganic phosphate, presumably through the back door. To further substantiate this hypothesis, we conducted a phosphate release assay revealing a reduction in phosphate release from polymerized F-actin when SipA was present (Fig. 6C). Together, our data suggest that a coordinated interplay of SipC with SipA leads to the decoration of young actin filaments by SipA, followed by stabilization of the actin filaments through intersubunit binding of the C-terminal arm of SipA. This stabilization process also involves delaying phosphate release through the closure of the actin back door.

DISCUSSION

Here, we uncovered how the bacterial effector SipA acts as a strong stabilizer of F-actin: First, it binds F-actin in a unique pattern that is distinct from any other known actin binding molecule. Second, it uses multiple interface residues to interact with high affinity. Third, it prevents P$_i$ release and maintains F-actin in a young state, thus preventing F-actin severing by cofilin I. Last, it stabilizes F-actin even under substoichiometric conditions, which are expected during bacterial infection.

In summary, our findings allow us to propose an integrated model of the coordinated interplay between SipC and SipA,

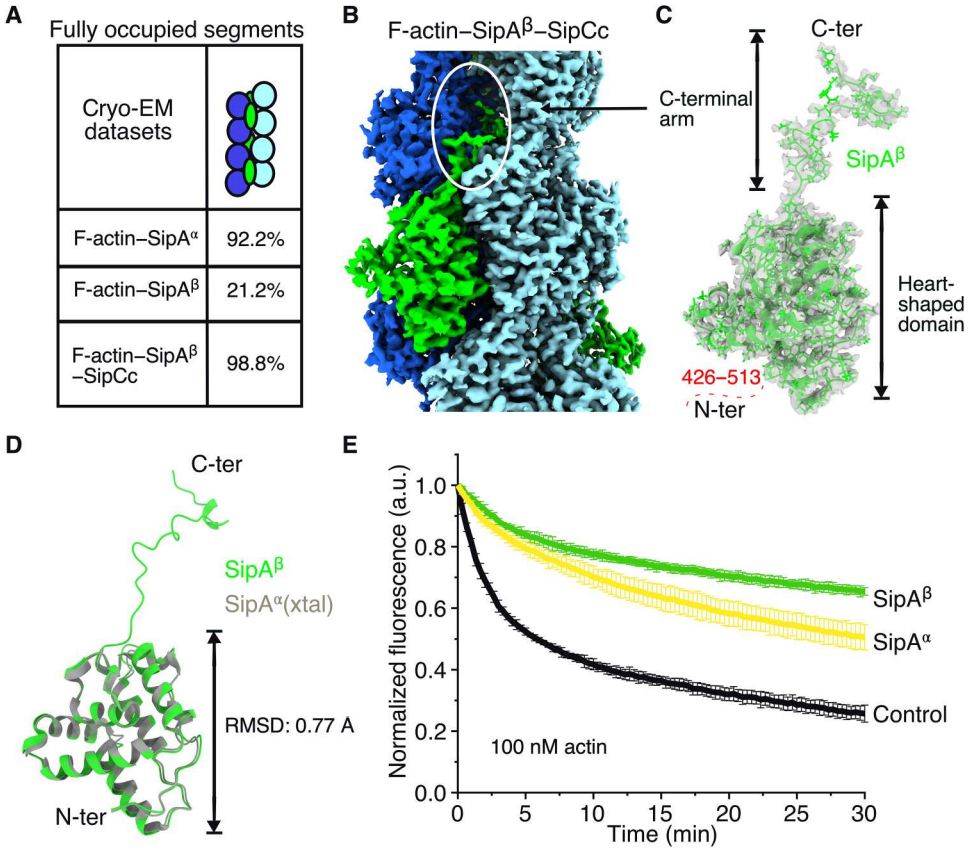

Fig. 5. SipC enhances SipA decoration of actin filaments and the extended arms contribute to F-actin stabilization. (**A**) The influence of SipCc on binding occupancy of SipA$^{\beta}$ on F-actin. A mask was generated to cover eight F-actin pockets where SipA can bind. This mask was then used for three-dimensional (3D) classification without alignment to calculate what fraction of F-actin segments used for 3D reconstruction was fully decorated. (**B**) Cryo-EM structure of F-actin–SipCc–SipA$^{\beta}$. The two helical strands of an actin filament polymerized in the presence of both SipCc and SipA$^{\beta}$ are colored in dark blue and light blue, respectively. No SipCc density was visible at any threshold level. (**C**) Extracted density of SipA$^{\beta}$ showing the fully resolved C-terminal (C-ter) arm. A model of SipA$^{\beta}$ (green) was built into the EM density map. The N-terminal (N-ter) arm was not visible in the reconstructed map. The C-terminal arm and the heart-shaped domain are indicated (*17*). (**D**) Comparison of SipA in the presence and absence of F-actin. The model of SipA$^{\beta}$ was aligned with the crystal structure of SipA$^{\alpha}$ (*17*) in ChimeraX 1.3. (**E**) Comparison of actin stabilization ability between SipA$^{\alpha}$ and SipA$^{\beta}$. Time course of F-actin depolymerization was induced by dilution in the presence of either 10 nM SipA$^{\alpha}$ or SipA$^{\beta}$. Solid lines indicate averages from three independent experiments, and error bars indicate SD.

which are sequentially secreted by the T3SS during the initial phase of host-pathogen interaction and manipulate the host cell actin cytoskeleton to facilitate *Salmonella* invasion of the host cell (Fig. 7). The secretion of the intermediate substrate SipC results in its anchoring as part of the translocon in the plasma membrane of the host cell. The actin-binding domain located at the C-terminal end of SipC nucleates actin filaments. The subsequently translocated substrate SipA is proteolytically cleaved within the host cell, releasing an actin-binding domain (*15*). This domain then binds to a specific site on the actin filament, a binding interaction that is enhanced in the vicinity of the infection site by SipC binding. SipA binding leads to the stabilization of young actin filaments, which is necessary for the reorganization of the cellular actin network at the site of infection. This reorganization facilitates the uptake of bacterial cells into the host cell and the progression of bacterial infection.

Several human ABPs, such as filamin A, T-plastin, and cofilin I, often have the same or overlapping binding sites located between two adjacent actin subunits along one actin-strand (Fig. 2D). However, the *Salmonella* effector SipA exploits a groove located between the two actin strands and extends to a neighboring binding pocket. These mutually exclusive binding sites ensure bacteria an efficient infection strategy by influencing the cytoskeleton independently of host ABPs. Still, some host actin-binding proteins such as actin depolymerizing factor (ADF)/cofilin are also required for efficient *Salmonella* entry by providing free G-actin for actin network assembly, which is further stabilized by SipA actin binding domain at *Salmonella* invasion sites (*3*, *32*). The binding of SipA is accomplished by a central globular domain and a flanking C-terminal domain, both of which are responsible for the unique binding pattern. The combined activity of SipA and the translocon protein SipC leads to stabilization of actin filaments. In this way, they influence the infection process, likely by locally stabilizing actin filaments at the T3SS-mediated interaction and injection site to form local membrane protrusions.

The fact that SipA primarily exerts its stabilizing effect on young actin filaments and even under substochiometric conditions underscores a highly effective mechanism at the host-pathogen interface.

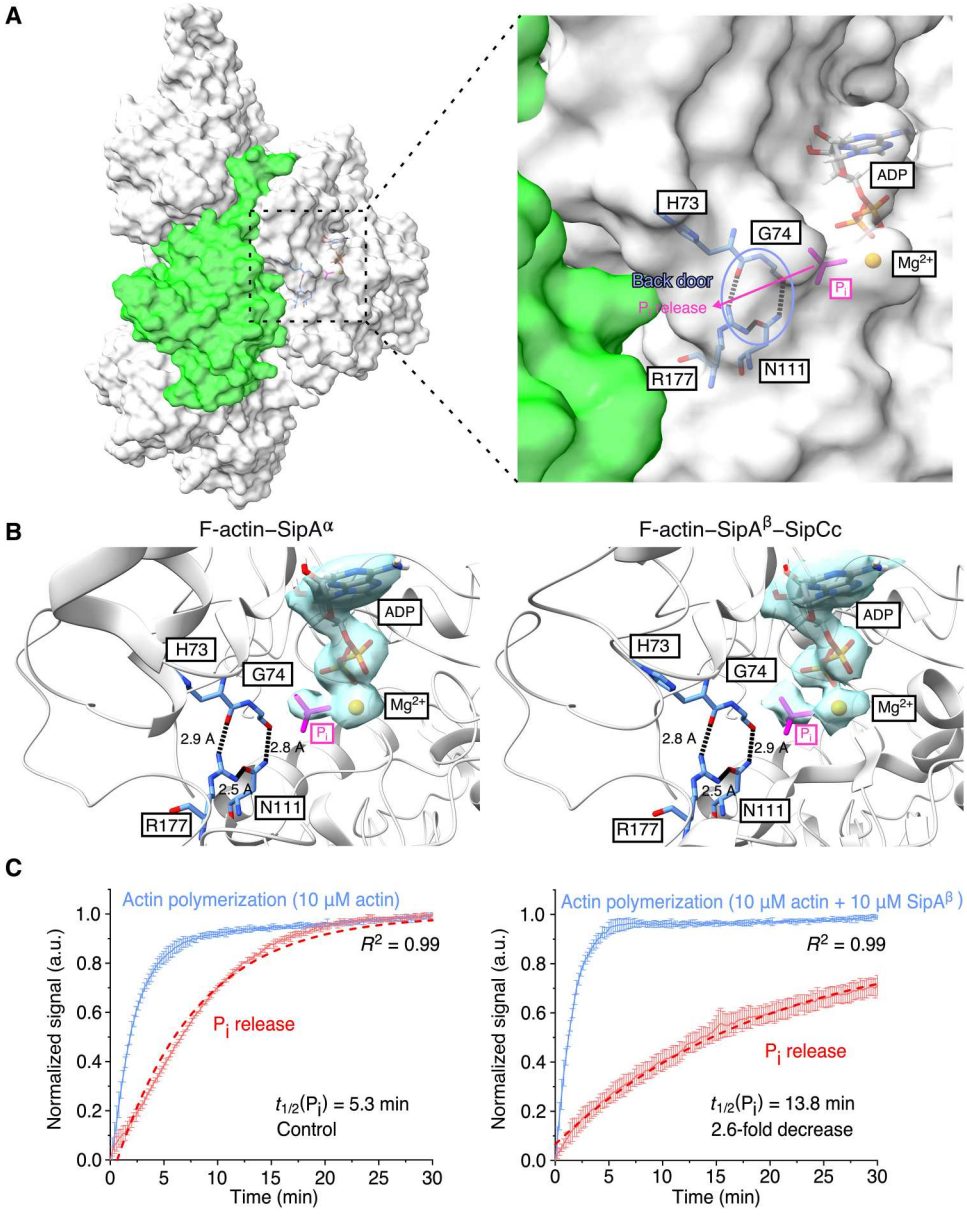

Fig. 6. SipA inhibits inorganic phosphate release during actin polymerization. (**A**) Overview of P_i release path from SipA–F-actin. The back door is formed by residues H73, G74, N111, and R177 and highlighted with a blue circle. (**B**) Comparison of the back doors of F-actin in presence of $SipA^{\alpha}$ (left), $SipA^{\beta}$, and SipCc (right). The EM density of ADP-P_i is shown in light blue. The lengths of the hydrogen bonds controlling the back door are indicated. P_i is colored in magenta. Residues: 301 to 313 and 154 to 161 are hidden to better visualize ADP-P_i and the back door residues. (**C**) $SipA^{\beta}$ blocks the back door of the actin nucleotide–binding site to interfere with release of inorganic phosphate during actin polymerization. Time courses of the normalized fluorescence intensities from 10 μM actin (1% pyrene-labeled) in the absence (left) or presence (right) of 10 μM $SipA^{\beta}$ (blue) and normalized absorbance of the P_i sensor product 2-amino-6-mercapto-7-methyl-purine (red) spiked with 250 nM F-actin seeds after initiation of the polymerization reaction. Solid lines indicate averages from four independent experiments, and error bars indicate SD. The red dashed lines correspond to monoexponential fits of the P_i release data (see Methods). R^2 indicates goodness of the fits. Corresponding half-lives of P_i release are indicated.

In the future, the unique nature of the binding mechanism of SipA to F-actin that we have identified here could make it possible to specifically inhibit this process and thereby interfere with *Salmonella* invasion of host cells. This could, in turn, lead to novel therapeutic approaches for treatment of *Salmonella* infections.

METHODS

Constructs, bacteria, and growth conditions

The strains and plasmids used in this study are listed in table S3. All bacteria strains were grown in LB medium. For the expression of *Salmonella* proteins in *Escherichia coli*, SipA and SipC fragments were amplified from *Salmonella* SB905 genomic DNA and subcloned into the pET52b-TEV-His and pPROEX-His-TEV vectors, respectively, using Gibson assembly. The DNA fragment of $SipA^{\beta}$

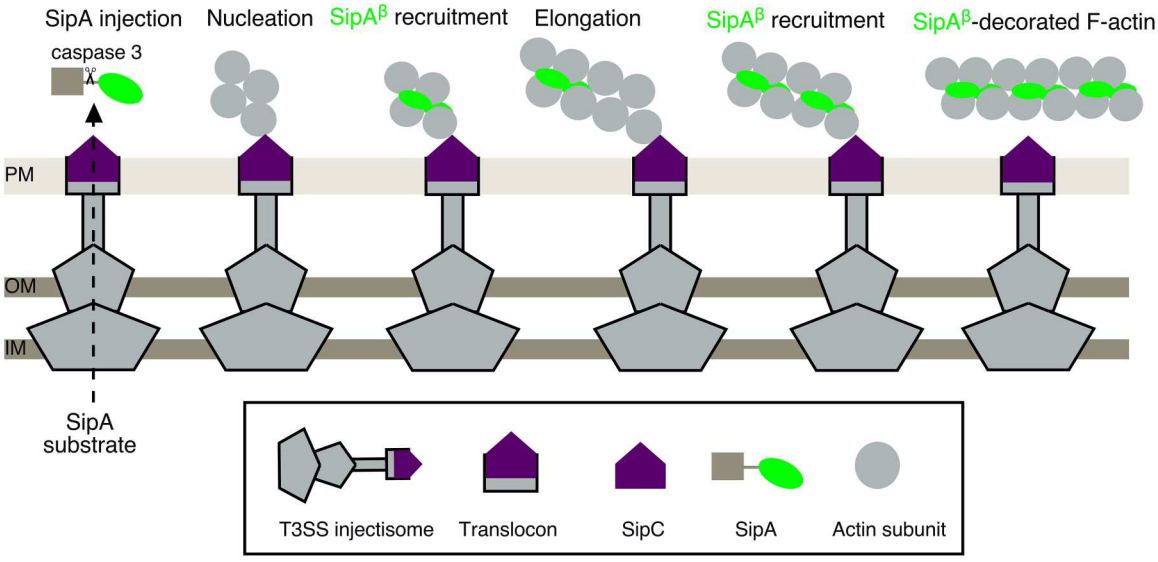

Fig. 7. Scheme of the possible cooperation mechanism between SipA and SipC in actin assembly at the *Salmonella* invasion site. PM, host cell plasma membrane; OM, bacterial outer membrane; IM, bacterial inner membrane.

encoding residues 426 to 685 was cloned into pGEX-6P1-SNAP vector (*33*) to make a SNAP-SipA$^{\beta}$ fusion using Gibson assembly, which allows the purification of glutathione *S*-transferase (GST)–SNAP-tag fusions and subsequent labeling of the SNAP-tag with fluorophores. Constructs for expression of SipA variant proteins were generated by polymerase chain reaction mutagenesis.

For the expression of GST-tagged proteins in *E. coli*, the cDNA of human full-length α-actinin 4 was amplified from the NIH 3T3 cDNA library (Invitrogen) and inserted into the Sal I–Not sites of pGEX-6P3 (GE Healthcare). For the expression of SNAP-tagged human T-plastin the full-length cDNA was amplified from the B16-F1 cDNA library and inserted between the Bam HI–Sal sites of pGEX-6P1-SNAP.

Salmonella strains with mutations in *sipA* were generated by using pORTMAGE (*34*). All expression constructs and *Salmonella* mutant strains were verified by DNA sequencing.

Purification and labeling of proteins

His-tagged proteins (table S3) were expressed in BL21(DE3) cells. The cultures were grown at 37°C with shaking until optical density at 600 nm (OD_{600}) = 0.8. Expression was induced by the addition of isopropyl-β-D-thiogalactopyranoside to a final concentration of 0.2 mM and the cultures were further grown overnight at 18°C. Cells were harvested by centrifugation at 4000*g* for 15 min, then resuspended in buffer containing 50 mM tris-HCl (pH 8.0), 300 mM NaCl, and 5% (v/v) glycerol, and then lysed by ultrasonication for 15 min (QSONICA, part no. Q500; 5-s on; 30-s off; 50% amplitude) on ice. Insoluble material was removed by centrifugation at 100,000*g* for 30 min at 4°C. The cell lysate supernatant was passed through a Ni^{+2}–nitrilotriacetic acid resin column (QIAGEN), and protein was purified following the manufacturer's instructions. His-tagged TEV protease was added to the eluted protein in a mass ratio of 1:100 and dialyzed against buffer containing 50 mM tris-HCl (pH 8.0) and 150 mM NaCl at 4°C overnight. The sample was passed through Ni^{+2}–nitrilotriacetic acid resin again to remove cleaved His-tag and TEV protease and then subjected to size exclusion chromatography using a Superdex 200 10/300 GL column (Cytiva). Fractions corresponding to A_{280} absorbance peaks were collected, concentrated to 3 to 5 mg/ml, aliquoted in 50 μl, flash-frozen in liquid nitrogen, and stored at −80°C.

GST-fusion proteins were expressed in *E. coli* host Rosetta 2 (Novagen). Expression was induced with 0.75 mM isopropyl-β-D-thiogalactopyranoside at OD_{600} = 0.8 at 21°C for 12 hours. The bacteria were harvested by centrifugation and lysed by ultrasonication as above in lysis buffer containing 30 mM Hepes (pH 7.4), 150 mM KCl, 2 mM EDTA, 1 mM dithiothreitol (DTT), 5% (v/v) glycerol, and benzonase (2 U/ml; Merck Millipore). The proteins were subsequently purified from bacterial extracts by affinity chromatography using glutathione-conjugated agarose 4B (Macherey-Nagel) using standard procedures. The GST-tag was cleaved off using PreScission protease (GE Healthcare), and the GST tag absorbed on fresh glutathione-conjugated agarose. The proteins in the flow through were further purified by size exclusion chromatography with HiLoad 26/600 Superdex 75 or 200 columns controlled by an Äkta Purifier System (Cytiva). The purification of human EGFP-tagged cofilin has been described (*19*, *35*). Ca^{2+}-ATP actin was purified from rabbit skeletal muscle according to Spudich and Watt (*36*), stored in G buffer [5 mM tris-HCl (pH 8.0), 0.2 mM $CaCl_2$, 0.5 mM DTT, and 0.2 mM ATP], and labeled on Cys374 with respective Atto maleimide dyes (ATTO-TEC) for TIRF microscopy assays or with *N*-(1-pyrenyl)-maleimide (Sigma-Aldrich) for F-actin depolymerization assays. SNAP-tagged constructs were labeled with either SNAP-Surface 488 or SNAP-Surface 549 following the protocol of the manufacturer (New England Biolabs). Unbound dye was removed by 2-ml Zeba desalting spin columns (Thermo Fisher Scientific).

Dilution-induced actin depolymerization assays

For actin depolymerization assays, 10 μM G-actin (50% pyrene-labeled) was polymerized in 1× KMEI [50 mM KCl, 1 mM $MgCl_2$, 1 mM EGTA, and 10 mM imidazole (pH 7.0)] at 4°C overnight. The resulting F-actin was prediluted to 0.8 μM in 1× KMEI

and placed in the automated dispenser of a Synergy 4 fluorescence microplate reader (BioTek). SipA constructs were then diluted to various concentrations in 1× KMEI buffer in a volume of 175 µl and then transferred into untreated black flat-bottomed 96-well microtiter plates. Dilution-induced depolymerization of F-actin was initiated by injecting 25 µl of the F-actin solution into each well of the microtiter plate, followed by a two second mixing step. The decrease in pyrene fluorescence was monitored with an excitation wavelength of 340 nm and an emission wavelength of 400 nm for 30 min. The data were normalized to 100%.

Immunofluorescence microscopy

HeLa cells (American Type Culture Collection CCL-2) were seeded onto eight-well chamber slides (Ibidi, Germany) in Dulbecco's modified Eagle's medium supplemented with 10% fetal bovine serum and grown to 70 to 80% confluency (5% CO_2 at 37°C). Cells were infected for 15 min with derivatives from *S. typhimurium* SL1344 at a multiplicity of infection of 5. Then, the cells were fixed with 4% paraformaldehyde in phosphate-buffered saline for 30 min at room temperature (RT). After quenching with 100 mM NH_4Cl, the cells were permeabilized for 30 min with permeabilization buffer (0.1% Triton X-100, 3% bovine serum albumin, and 1× phosphate-buffered saline). The samples were then stained for 1 hour at RT with mouse anti-HA antibodies (1:500; anti-HA.11 epitope tag antibody, MMS-101R, BioLegend, Germany), followed by washing and incubation with the secondary goat anti-mouse AF488 antibodies (1:500; Thermo Fisher Scientific), Atto-647N–conjugated phalloidin (1:100; ATTO-TEC, Germany), and DAPI (4′,6-diamidino-2-phenylindole; 1:1000, Thermo Fisher Scientific) as indicated. Images were obtained using a Nikon Eclipse Ti2 spinning disc microscope equipped with a 100× numerical aperture of 1.49 plan apochromat oil immersion objective, a Yokogawa CSU-W1 spinning disc unit, and an Andor iXon Ultra 888 electron multiplying charge-coupled device camera.

Cosedimentation assay

G-actin was prepared from chicken muscle (*36*), with a final purification step using HiLoad 16/600 Superdex 200 column equilibrated with G-actin buffer. For cosedimentation assays, ABPs were first exchanged into buffer containing 25 mM tris-HCl (pH 8.0) and 2 mM DTT using a 10-kDa molecular weight cutoff centrifugal concentrator at 5000*g*. G-actin was centrifuged at 150,000*g* for 30 min to remove actin filaments or aggregates.

For the actin polymerization assay, G-actin and the ABP were mixed at final concentrations of 10 and 50 µM, respectively, in actin polymerization buffer A [5 mM Tris/HCl buffer (pH 8.0), 0.1 mM DTT, 0.2 mM ATP, 0.2 mM EGTA, and 0.05 mM $MgCl_2$] and incubated for 2 hours at RT, unless stated otherwise. Ultracentrifugation at 150,000*g* for 30 min was performed with an Optima MAX-XP ultracentrifuge to pellet F-actin, and the resulting pellet and supernatant fractions were brought to the same volume of SDS-sample buffer and analyzed by SDS–polyacrylamide gel electrophoresis (PAGE).

For the F-actin binding assay, G-actin was polymerized in F-actin binding buffer B [25 mM Tris/HCl (pH 8.0), 100 mM KCl, 2 mM $MgCl_2$, 1 mM ATP, and 1 mM DTT] for 1 hour at RT. Polymerized F-actin was obtained by ultracentrifugation at 150,000*g* for 30 min. F-actin was resuspended in buffer B. Then, F-actin and the ABP were mixed and incubated at RT for 2 hours. Ultracentrifugation at 150,000*g* for 30 min was performed to pellet F-actin, and the resulting fractions were analyzed by SDS-PAGE.

Cryo-EM data acquisition and processing

F-actin and ABP complexes were vitrified on Quantifoil 300- or 200-mesh 2.0/1.0 grids. Briefly, 4 µl of the sample was applied onto glow-discharged grids (glow discharge conditions, negative; 25 mA for 1.5 to 2 min). The grids were blotted for 3 to 5 s (blot force, −5 to 0; 100% humidity) and plunge-frozen in liquid ethane/propane mix using a Vitrobot Mark IV (FEI). The vitrified specimens were imaged on an FEI Titan Krios operating at 300 kV and equipped with a Gatan K3 camera running in counting mode and using Thermo Fisher Scientific EPU software. Movies were recorded with a nominal magnification of ×105,000, corresponding to a pixel size of 0.826 Å at the specimen level. Movies were recorded with a defocus range of 0.8 to 3.0 µm. For individual frames, an electron dose of 1.4 e/A^2 was used. Corresponding to a cumulative electron dose of 56 e/A^2 equally distributed over a 3-s movie.

Single-particle helical reconstruction was performed using Relion 3.1 (*37*). Movies were motion-corrected using MotionCor2 (*38*). The contrast transfer function (CTF) of the resulting micrographs was estimated using CTFFIND4 (*39*). Particle picking was performed using cryolo 1.7 (*40*). The helical segments were extracted into 512 × 512 boxes and subsequently binned by four and split into four datasets. A clean dataset was obtained by combining these four datasets after two-dimensional (2D) classification. 3D classification and autorefinement with initial helical parameters of a helical rise of 27.3 Å and a helical twist of −166.5° were performed with local searches of helical symmetry. The 3D classes that showed clear F-actin features were combined and used for further 3D autorefinement. To improve the SipA density, a mask was generated around the SipA density and used for classification without alignment. The class with the best EM density for SipA was then chosen for the final 3D autorefinement. Overall, gold-standard resolution (Fourier shell correlation = 0.143) and local resolution were calculated in Relion 3.1. The statistics for data collection and processing are listed in table S4.

Model building and refinement

Previously built models of F-actin [Protein Data Bank (PDB): 5ONV] (*41*) and SipA (PDB: 1Q5Z) (*17*) were used as initial models. Models were built in ChimeraX 1.3 (*42*), and interactive refinement against the cryo-EM maps was performed with ISOLDE (*43*). The resulting coordinate files were further refined with real-space refinement in Phenix (*44*). Model validation was carried out using the MolProbity server (*45*) and EMRinger (*46*). The parameters of the final models are described in table S4.

Preparation of lipid vesicles

1,2-dioleoyl-*sn*-glycero-3-phosphocholine (DOPC) in chloroform was purchased from Avanti Polar Lipids. Unilamellar lipid vesicles composed of DOPC were prepared by extrusion using an Avanti Mini Extruder (Avanti Polar Lipids). The solvent in stock solutions of DOPC was evaporated with a stream of dry nitrogen for 1 hour. The dried lipids were resuspended in unilamellar lipid vesicle buffer containing 20 mM Hepes, 150 mM NaCl, 5 mM KCl, 3 mM $MgCl_2$, and 5 mM β-mercaptoethanol (pH 7.4) at a total lipid concentration of 2 mg/ml, then sonicated for 3 min using a tapered microtip

creating a turbid suspension, and lastly extruded 15 times through a 100-nm polycarbonate membrane (Avanti Polar Lipids) yielding small unilamellar vesicles.

In vitro TIRF microscopy

Glass coverslips were precleaned with 50°C warm, double-distilled H_2O containing 2% (v/v) Hellmanex III for 30 min and then rinsed with double-distilled H_2O, followed by equivalent steps using 1 M KOH, 1 M HCl, and 70% ethanol, respectively. Dried coverslips were subsequently treated with room air plasma using an expanded table-top plasma cleaner (Harrick Plasma) for 30 min.

Two-channel TIRF flow chambers were prepared by attaching the cleaned coverslips to glass slides using three small stripes of double-sided tape. Before the experiments, the channels were first filled with 20 µl of the lipid vesicle solution to form supported lipid bilayers on the solid glass surface within 30 min and then rinsed twice with 1× KMEI buffer supplemented with 1% bovine serum albumin.

Reactions in TIRF assays contained 1 µM actin (spiked with 15 to 20% Atto488, Atto550, or Atto655, respectively). Before the experiments, Ca^{2+}-ATP-actin was converted to Mg^{2+}-ATP-actin by addition of 10× magnesium-exchange buffer [1 mM $MgCl_2$ and 10 mM EGTA (pH 7.4)]. Polymerization experiments were performed in TIRF buffer containing 10 mM imidazole, 50 mM KCl, 1 mM $MgCl_2$, 1 mM EGTA, 0.2 mM ATP, 10 mM DTT, 15 mM glucose, catalase (20 µg/ml), glucose oxidase (100 µg/ml), and 0.5% methylcellulose (4000 cP) (pH 7.4). The TIRF microscopy assays were initiated by addition of ATP–G-actin and by flushing the mixtures into prepared flow chambers. Images were captured with a Nikon Eclipse TI-E inverted microscope equipped with a CFI Apochromat TIRF 100× oil, numerical aperture of 1.49 objective using 488-, 561-, and 640-nm laser lines at 5-s intervals with exposure times of 70 ms by Ixon3 897 electron multiplying charge-coupled device cameras (Andor) for 15 to 20 min. The pixel size corresponded to 0.159 µm. The elongation rates of filaments were determined by manual tracking of growing barbed ends using ImageJ software (*47*). At least 30 filaments were measured from three independent movies per condition for the experiments in the presence of $SipA^{\beta}$ and the actin control experiments. For comparison of nucleation efficacies, the average number of filaments was obtained by counting all actin filaments in an area of 50 µm by 50 µm for 300 s after initiation of the polymerization reaction in three independent movies per condition.

Simultaneous measurement of actin polymerization and P_i release in bulk assays

Phosphate release assays were carried out by combining seeded pyrene actin polymerization assays with the EnzChek Phosphate Assay Kit (Invitrogen) to simultaneously monitor bulk actin polymerization and release of P_i. For the generation of seeds, 10 µM G-actin were first polymerized in 1× KMEI at 4°C overnight. To remove P_i from ADP-F-actin, the filaments were subsequently centrifuged at 150,000*g* at 4°C for 45 min, and the pellet was washed once with 1× KMEI, followed by resuspending the pellet in 1× KMEI yielding a 5 µM ADP–F-actin solution. Immediately before use, the F-actin solution was sonicated in an ultrasonic bath for 5 min to generate the F-actin seeds. On the day of the experiment, Ca^{2+}-ATP–G-actin was run over a HiLoad 26/600 Superdex 75 size exclusion chromatography column equilibrated in G-buffer devoid of ATP to remove potential P_i impurities and unbound nucleotide, taking into account that spontaneous ATP hydrolysis of Ca^{2+}-ATP–G-actin is slow. Ca^{2+}-ATP–G-actin was then spiked with 1% pyrene-labeled G-actin and diluted to 44.44 µM using ATP-free G-buffer. The pyrene–G-actin solution was then mixed at a ratio of 1:10 with 10× ME [5 mM EGTA (pH 7.5) and 1 mM $MgCl_2$] and incubated for 2 min on ice, yielding a 40 µM Mg^{2+}-ATP–G-actin solution. For each measurement, 13.33 µM $SipA^{\beta}$ or the same volume of SipA-storage buffer (negative control), 266.67 µM 2-amino-6-mercapto-7-methyl-purine riboside (MESG), 1 U of purine nucleoside phosphorylase (PNP), and 333 nM of freshly prepared F-actin seeds were diluted in 150 µl of 1.33× KMEI and transferred in untreated black flat-bottomed 96-well microtiter plates with a transparent bottom. The mixture was incubated for 10 min at RT to reduced residual P_i contaminations using the MESG/PNP reaction as a P_i mop as suggested by the manufacturer's protocol. The assembly reaction was initiated by injection of 50 µl of Mg^{2+}-ATP–G-actin solution into the protein mixture to reach a final concentration of 10 µM actin, 0 or 10 µM $SipA^{\beta}$, 200 µM MESG, 1 U of PNP, 250 nM F-actin seeds in 1× KMEI by the automated dispenser of a Synergy 4 fluorescence microplate reader (BioTek). The increase in pyrene fluorescence was monitored with an excitation wavelength of 340 nm and an emission wavelength of 400 nm. P_i release was monitored by measuring the absorbance of the P_i sensor product MESG at 360 nm.

Time courses of pyrene fluorescence and absorbance of the P_i sensor product from individual experiments were first normalized by subtracting the minimal signal at the beginning of the experiment and dividing by the maximal signal at saturation. Apparent half-lives of P_i release were then determined by fitting averaged data from four independent experiments by the monoexponential function in Origin 2021 software (OriginLab)

$$A(t) = A^{*}e^{-\frac{\ln(2)}{t_{1/2}}*t} + y_0$$

where $A(t)$ is the absorbance of the P_i sensor product over time (t), $t_{1/2}$ is the apparent half-life of the P_i release, A is the amplitude, and y_0 is the offset of the exponential function.

Statistical analysis

Quantitative experiments were performed at least in triplicates except for cryo-EM datasets. Statistical analyses were performed using GraphPad Prism 9 (GraphPad, San Diego, CA) and Origin 2021 software (OriginLab). Statistical differences between the two groups were determined by the *t* test with the unpaired experimental design of the two groups by the nonparametric Mann-Whitney test. Statistical differences were defined as $^{*}P \leq 0.05$, $^{**}P \leq 0.01$, $^{***}P \leq 0.001$, and ns (not significant).

Supplementary Materials

This PDF file includes:

Figs. S1 to S6
Legends for movies S1 to S7
Tables S1 to S4

Other Supplementary Material for this manuscript includes the following:

Movies S1 to S7

REFERENCES AND NOTES

1. T. D. Pollard, Actin and actin-binding proteins. *Cold Spring Harb. Perspect. Biol.* **8**, a018226 (2016).
2. A. P. Bhavsar, J. A. Guttman, B. B. Finlay, Manipulation of host-cell pathways by bacterial pathogens. *Nature* **449**, 827–834 (2007).
3. E. J. McGhie, R. D. Hayward, V. Koronakis, Control of actin turnover by a Salmonella invasion protein. *Mol. Cell* **13**, 497–510 (2004).
4. Y. Fu, J. E. Galán, A Salmonella protein antagonizes Rac-1 and Cdc42 to mediate host-cell recovery after bacterial invasion. *Nature* **401**, 293–297 (1999).
5. D. Liebl, X. Qi, Y. Zhe, T.C. Barnett, R.D. Teasdale, SopB-Mediated Recruitment of SNX18 Facilitates Salmonella Typhimurium Internalization by the Host Cell. *Front. Cell. Infect. Microbiol.* **7**2017).
6. E. J. McGhie, R. D. Hayward, V. Koronakis, Cooperation between actin-binding proteins of invasive Salmonella: SipA potentiates SipC nucleation and bundling of actin. *EMBO J.* **20**, 2131–2139 (2001).
7. B. C. Russo, J. K. Duncan, M. B. Goldberg, Topological analysis of the type 3 secretion system translocon pore protein IpaC following its native delivery to the plasma membrane during infection. *MBio* **10**, e00877-19 (2019).
8. D. Park, M. Lara-Tejero, M. N. Waxham, W. Li, B. Hu, J. E. Galán, J. Liu, Visualization of the type III secretion mediated *Salmonella*–host cell interface using cryo-electron tomography. *eLife* **7**, e39514 (2018).
9. R. D. Hayward, V. Koronakis, Direct nucleation and bundling of actin by the SipC protein of invasive Salmonella. *EMBO J.* **18**, 4926–4934 (1999).
10. S. K. Myeni, D. Zhou, The C terminus of SipC binds and bundles F-actin to promote Salmonella invasion. *J. Biol. Chem.* **285**, 13357–13363 (2010).
11. C. D. Nichols, J. E. Casanova, Salmonella-directed recruitment of new membrane to invasion foci via the host exocyst complex. *Curr. Biol.* **20**, 1316–1320 (2010).
12. R. Madan, R. Rastogi, S. Parashuraman, A. Mukhopadhyay, Salmonella acquires lysosome-associated membrane protein 1 (LAMP1) on phagosomes from golgi via SipC protein-mediated recruitment of host Syntaxin6. *J. Biol. Chem.* **287**, 5574–5587 (2012).
13. W. Deng, N. C. Marshall, J. L. Rowland, J. M. McCoy, L. J. Worrall, A. S. Santos, N. C. J. Strynadka, B. B. Finlay, Assembly, structure, function and regulation of type III secretion systems. *Nat. Rev. Microbiol.* **15**, 323–337 (2017).
14. A. McIntosh, L. M. Meikle, M. J. Ormsby, B. A. McCormick, J. M. Christie, J. M. Brewer, M. Roberts, D. M. Wall, SipA activation of caspase-3 is a decisive mediator of host cell survival at early stages of *Salmonella enterica* serovar typhimurium infection. *Infect. Immun.* **85**, e00393-17 (2017).
15. C. V. Srikanth, D. M. Wall, A. Maldonado-Contreras, H. N. Shi, D. Zhou, Z. Demma, K. L. Mumy, B. A. McCormick, *Salmonella* pathogenesis and processing of secreted effectors by caspase-3. *Science* **330**, 390–393 (2010).
16. P. K. Singh, A. Kapoor, R. M. Lomash, K. Kumar, S. C. Kamerkar, T. J. Pucadyil, A. Mukhopadhyay, Salmonella SipA mimics a cognate SNARE for host Syntaxin8 to promote fusion with early endosomes. *J. Cell Biol.* **217**, 4199–4214 (2018).
17. M. Lilic, V. E. Galkin, A. Orlova, M. S. VanLoock, E. H. Egelman, C. E. Stebbins, *Salmonella* SipA polymerizes actin by stapling filaments with nonglobular protein arms. *Science* **301**, 1918–1921 (2003).
18. V. E. Galkin, A. Orlova, M. S. VanLoock, D. Zhou, J. E. Galán, E. H. Egelman, The bacterial protein SipA polymerizes G-actin and mimics muscle nebulin. *Nat. Struct. Mol. Biol.* **9**, 518–521 (2002).
19. D. Breitsprecher, S. A. Koestler, I. Chizhov, M. Nemethova, J. Mueller, B. L. Goode, J. V. Small, K. Rottner, J. Faix, Cofilin cooperates with fascin to disassemble filopodial actin filaments. *J. Cell Sci.* **124**, 3305–3318 (2011).
20. B. Winnen, M. C. Schlumberger, A. Sturm, K. Schüpbach, S. Siebenmann, P. Jenny, W.-D. Hardt, Hierarchical effector protein transport by the Salmonella typhimurium SPI-1 type iii secretion system. *PLOS ONE* **3**, e2178 (2008).
21. M. C. Schlumberger, A. J. Müller, K. Ehrbar, B. Winnen, I. Duss, B. Stecher, W.-D. Hardt, Real-time imaging of type III secretion: Salmonella SipA injection into host cells. *Proc. Natl. Acad. Sci. U.S.A.* **102**, 12548–12553 (2005).
22. L. C. Brawn, R. D. Hayward, V. Koronakis, Salmonella SPI1 effector SipA persists after entry and cooperates with a SPI2 effector to regulate phagosome maturation and intracellular replication. *Cell Host Microbe* **1**, 63–75 (2007).
23. G. Erdős, M. Pajkos, Z. Dosztányi, IUPred3: Prediction of protein disorder enhanced with unambiguous experimental annotation and visualization of evolutionary conservation. *Nucleic Acids Res.* **49**, W297–W303 (2021).
24. A. Kumari, S. Kesarwani, M. G. Javoor, K. R. Vinothkumar, M. Sirajuddin, Structural insights into actin filament recognition by commonly used cellular actin markers. *EMBO J.* **39**, e104006 (2020).
25. Z. Wang, M. Grange, S. Pospich, T. Wagner, A. L. Kho, M. Gautel, S. Raunser, Structures from intact myofibrils reveal mechanism of thin filament regulation through nebulin. *Science* **375**, eabn1934 (2022).
26. L. Mei, M. J. Reynolds, D. Garbett, R. Gong, T. Meyer, G. M. Alushin, Structural mechanism for bidirectional actin cross-linking by T-plastin. *Proc. Natl. Acad. Sci. U.S.A.* **119**, e2205370119 (2022).
27. D. V. Iwamoto, A. Huehn, B. Simon, C. Huet-Calderwood, M. Baldassarre, C. V. Sindelar, D. A. Calderwood, Structural basis of the filamin A actin-binding domain interaction with F-actin. *Nat. Struct. Mol. Biol.* **25**, 918–927 (2018).
28. A. R. Huehn, J. P. Bibeau, A. C. Schramm, W. Cao, E. M. De La Cruz, C. V. Sindelar, Structures of cofilin-induced structural changes reveal local and asymmetric perturbations of actin filaments. *Proc. Natl. Acad. Sci. U.S.A.* **117**, 1478–1484 (2020).
29. E. M. De La Cruz, Cofilin binding to muscle and non-muscle actin filaments: Isoform-dependent cooperative interactions. *J. Mol. Biol.* **346**, 557–564 (2005).
30. W. Oosterheert, B. U. Klink, A. Belyy, S. Pospich, S. Raunser, Structural basis of actin filament assembly and aging. *Nature* **611**, 374–379 (2022).
31. M. J. Reynolds, C. Hachicho, A. G. Carl, R. Gong, G. M. Alushin, Bending forces and nucleotide state jointly regulate F-actin structure. *Nature* **611**, 380–386 (2022).
32. S. Dai, P. D. Sarmiere, O. Wiggan, J. R. Bamburg, D. Zhou, Efficient Salmonella entry requires activity cycles of host ADF and cofilin. *Cell. Microbiol.* **6**, 459–471 (2004).
33. M. Winterhoff, A. Junemann, B. Nordholz, J. Linkner, M. Schleicher, J. Faix, The Diaphanous-related formin dDia1 is required for highly directional phototaxis and formation of properly sized fruiting bodies in Dictyostelium. *Eur. J. Cell Biol.* **93**, 212–224 (2014).
34. Á. Nyerges, B. Csörgő, I. Nagy, B. Bálint, P. Bihari, V. Lázár, G. Apjok, K. Umenhoffer, B. Bogos, G. Pósfai, C. Pál, A highly precise and portable genome engineering method allows comparison of mutational effects across bacterial species. *Proc. Natl. Acad. Sci. U.S.A.* **113**, 2502–2507 (2016).
35. F. P. L. Lai, M. Szczodrak, J. Block, J. Faix, D. Breitsprecher, H. G. Mannherz, T. E. B. Stradal, G. A. Dunn, J. V. Small, K. Rottner, Arp2/3 complex interactions and actin network turnover in lamellipodia. *EMBO J.* **27**, 982–992 (2008).
36. J. A. Spudich, S. Watt, The regulation of rabbit skeletal muscle contraction. *J. Biol. Chem.* **246**, 4866–4871 (1971).
37. J. Zivanov, T. Nakane, B. O. Forsberg, D. Kimanius, W. J. Hagen, E. Lindahl, S. H. Scheres, New tools for automated high-resolution cryo-EM structure determination in RELION-3. *eLife* **7**, e42166 (2018).
38. S. Q. Zheng, E. Palovcak, J.-P. Armache, K. A. Verba, Y. Cheng, D. A. Agard, MotionCor2: Anisotropic correction of beam-induced motion for improved cryo-electron microscopy. *Nat. Methods* **14**, 331–332 (2017).
39. A. Rohou, N. Grigorieff, CTFFIND4: Fast and accurate defocus estimation from electron micrographs. *J. Struct. Biol.* **192**, 216–221 (2015).
40. T. Wagner, F. Merino, M. Stabrin, T. Moriya, C. Antoni, A. Apelbaum, P. Hagel, O. Sitsel, T. Raisch, D. Prumbaum, D. Quentin, D. Roderer, S. Tacke, B. Siebolds, E. Schubert, T. R. Shaikh, P. Lill, C. Gatsogiannis, S. Raunser, SPHIRE-crYOLO is a fast and accurate fully automated particle picker for cryo-EM. *Commun. Biol.* **2**, 218 (2019).
41. F. Merino, S. Pospich, J. Funk, T. Wagner, F. Küllmer, H.-D. Arndt, P. Bieling, S. Raunser, Structural transitions of F-actin upon ATP hydrolysis at near-atomic resolution revealed by cryo-EM. *Nat. Struct. Mol. Biol.* **25**, 528–537 (2018).
42. E. F. Pettersen, T. D. Goddard, C. C. Huang, E. C. Meng, G. S. Couch, T. I. Croll, J. H. Morris, T. E. Ferrin, UCSF ChimeraX : Structure visualization for researchers, educators, and developers. *Protein Sci.* **30**, 70–82 (2021).
43. T. I. Croll, ISOLDE: A physically realistic environment for model building into low-resolution electron-density maps. *Acta Crystallogr. D Struct. Biol.* **74**, 519–530 (2018).
44. D. Liebschner, P. V. Afonine, M. L. Baker, G. Bunkóczi, V. B. Chen, T. I. Croll, B. Hintze, L.-W. Hung, S. Jain, A. J. McCoy, N. W. Moriarty, R. D. Oeffner, B. K. Poon, M. G. Prisant, R. J. Read, J. S. Richardson, D. C. Richardson, M. D. Sammito, O. V. Sobolev, D. H. Stockwell, T. C. Terwilliger, A. G. Urzhumtsev, L. L. Videau, C. J. Williams, P. D. Adams, Macromolecular structure determination using X-rays, neutrons and electrons: Recent developments in *Phenix*. *Acta Crystallogr. D Struct. Biol.* **75**, 861–877 (2019).
45. C. J. Williams, J. J. Headd, N. W. Moriarty, M. G. Prisant, L. L. Videau, L. N. Deis, V. Verma, D. A. Keedy, B. J. Hintze, V. B. Chen, S. Jain, S. M. Lewis, W. B. Arendall, J. Snoeyink, P. D. Adams, S. C. Lovell, J. S. Richardson, D. C. Richardson, MolProbity: More and better reference data for improved all-atom structure validation. *Protein Sci.* **27**, 293–315 (2018).
46. B. A. Barad, N. Echols, R. Y.-R. Wang, Y. Cheng, F. DiMaio, P. D. Adams, J. S. Fraser, EMRinger: Side chain–directed model and map validation for 3D cryo-electron microscopy. *Nat. Methods* **12**, 943–946 (2015).
47. C. A. Schneider, W. S. Rasband, K. W. Eliceiri, NIH image to ImageJ: 25 years of image analysis. *Nat. Methods* **9**, 671–675 (2012).

Acknowledgments: We thank all members of the Marlovits laboratory for support of this project. We thank T. Paraschiakos for providing chicken muscle acetone powder. The data processing was performed at the German Electron Synchrotron Centre (DESY) using the High-Performance Computing Cluster. **Funding:** This project was supported by funds available to T. C.M. through the Behörde für Wissenschaft, Forschung und Gleichstellung of the city of Hamburg at the Institute of Structural and Systems Biology at the University Medical Center Hamburg-Eppendorf (UKE) and Deutsches Elektronen Synchrotron (DESY). Additional support was provided through the following grants: DFG Fa330/12-3. Part of this work was performed at the Multi-User Cryo-EM Facility at the Centre for Structural Systems Biology, Hamburg, supported by the University of Hamburg and DFG grant numbers (INST 152/772-1, 152/774-1, 152/775-1, 152/776-1, and 152/777-1 FUGG). **Author contributions:** Investigation: B.Y., R.T., J.F., S.W., J.W., and T.C.M. designed the experiments. B.Y. generated constructs and *Salmonella* mutant strains and performed protein purification and actin cosedimentation assay. B.Y. and J. W. collected and processed cryo-EM data. B.Y. built the atomic models. B.Y. and R.T. performed infection assays and fluorescence microscopy imaging. J.S., B.Y., and I.E. performed actin depolymerization assay. J.S. performed TIRF assay and phosphate release assay. B.Y., R.H.J., S.W., J.F., and T.C.M. wrote and revised the paper. All authors read, corrected, and approved the manuscript. J.F. and S.W. supervised actin depolymerization assay. J.F. supervised the TIRF assay and phosphate release assay. T.C.M. conceived the study and supervised the project. **Competing interests:** The authors declare they have no competing interests. **Data and materials availability:** Models and associated EM maps have been deposited with the following accession numbers: F-actin−SipA$^{\alpha}$ (EMD-16424, PDB: 8C4C) and F-actin −SipA$^{\beta}$−SipCc (EMD-16425, PDB: 8C4E). All data needed to evaluate the conclusions in the paper are present in the paper and/or the Supplementary Materials.

Submitted 4 July 2023
Accepted 9 November 2023
Published 8 December 2023
10.1126/sciadv.adj5777